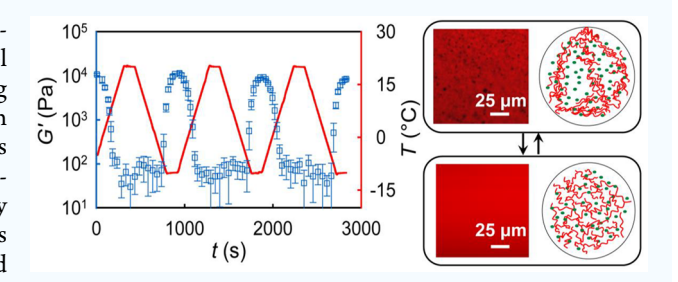
Crystallization-Arrested Viscoelastic Phase Separation in Semiconducting Polymer Gels

Jing He, Xiaoqing Kong, Yuhao Wang, Michael Delaney, Dilhan M. Kalyon, and Stephanie S. Lee*, To

Supporting Information

ABSTRACT: Through a combination of rheological characterization and temperature-variable imaging methods, a novel gelation pathway in dilute solutions of a semiconducting polymer to achieve interconnected, crystalline networks with hierarchical porosity is reported. Upon rapid cooling, solutions of regioregular poly(3-hexylthiophene) in ortho-dichlorobenzene formed thermoreversible gels. Confocal microscopy revealed cooling-induced structural rearrangement to progress through viscoelastic phase separation (VPS), which arrested prematurely during the formation of micron-sized solvent-rich



"holes" due to interchain crystallization. Cryogen-based scanning electron microscopy uncovered an interfibrillar network exhibiting nanosized pores. These networks formed to equal gel strengths when a third component, either small molecule phenyl- C_{61} -butyric acid methyl ester or noncrystallizing regiorandom, poly(3-hexylthiophene), was added to the solution. Organic solar cells deposited with active layers from phase-separated solutions displayed 45% higher efficiency compared to reference cells. The demonstrated ability to arrest VPS enables control over the morphology of porous materials for applications ranging from membrane filtration to plastic foam manufacturing.

KEYWORDS: viscoelastic phase separation, gelation, rheology, polymer crystallization, organic photovoltaics, cryo-SEM, confocal microscopy

■ INTRODUCTION

Viscoelastic phase separation (VPS), a thermodynamic phenomenon unique to systems in which there exists a dynamic asymmetry between the components, is a promising avenue to direct the self-assembly of materials into hierarchical structures.1 Unlike classical phase separation, VPS initiates through the formation of droplets of the fast-moving component, e.g. a small-molecule solvent, within a matrix of the slow-moving component, e.g., a long-chain polymer.²⁻⁴ If attractive molecular interactions are sufficiently strong in the slow-moving phase, the system will form a transient gel. Over time, the droplets of the fast-moving phase grow and coalesce to form the majority phase. However, if VPS is arrested in the transient gel phase, the formation of stable cellular and network structures is possible.

The arresting of the transient gel phase is likely responsible for naturally occurring network structures found in, for example, magma³ and foods.⁵ By evacuating the solvent during the early stages of VPS, and porous scaffolds for tissue engineering were formed from polymer blends exhibiting dynamic asymmetry between the two components. Crystallization-arrested VPS has also been observed in protein

solutions at high concentrations, resulting in the formation of stable gels.7 Recently, Tanaka and co-workers reported crystallization-arrested VPS in colloidal suspensions to form "crystal gels."8 This structure was achieved by inducing VPS below the melting point of colloid crystals, such that nucleation and crystal growth occurred during the formation of percolated networks of the liquid colloidal phase.

Here we demonstrate that the formation of porous crystalline networks via VPS presents a promising, scalable route to achieve optimized morphologies in the active layers of organic solar cells (OSCs). In these devices, the photoactive layer is typically deposited from a solution comprising a blend of an electron-donating polymer and electron-accepting small molecule. The compositions of these solutions with dynamically asymmetric components are typical of those that have been demonstrated to undergo VPS in the past. For the application of light energy harvesting, porous polymer networks exhibiting a large interfacial surface area with the

Received: December 5, 2018 Accepted: February 12, 2019 Published: February 12, 2019

[†]Department of Chemical Engineering and Materials Science, Stevens Institute of Technology, Hoboken, New Jersey 07030, United

[‡]Department of Biomedical Engineering, Stevens Institute of Technology, Hoboken, New Jersey 07030, United States

[§]Highly Filled Materials Institute, Stevens Institute of Technology, Hoboken, New Jersey 07030, United States

electron acceptor promote efficient exciton dissociation. Furthermore, polymer crystallization within these percolated networks facilitates efficient hole transport to the anode. Given that morphological control over the OSC active layers remains a critical challenge, ⁹ VPS is an intriguing avenue toward robust control over solution structures prior to active layer deposition.

Upon rapid cooling, VPS occurring in electron-donating (RR-P3HT) solutions leads to the formation of stable, crystalline RR-P3HT gel networks with hierarchical porosity that improve the light harvesting efficiency of solar cell active layers. A combination of rheological characterization and temperature-dependent fluorescence microscopy revealed that VPS is arrested during solvent hole formation due to interchain crystallization of RR-P3HT. This crystallization-induced gelation during VPS was found to be thermoreversible and remarkably insensitive to the presence of both PCBM and noncrystallizing regiorandom-P3HT (Rra-P3HT). Once formed in solution, these semicrystalline RR-P3HT networks can be transferred to OSC device platforms via doctor blading, a method compatible with continuous processing methods. OSCs comprising cooled photoactive layers displayed 45% higher efficiencies compared to those comprising uncooled photoactive layers. Through the discovery of a novel gelation mechanism in this extensively studied system, we thus present a viable strategy to control the photoactive layer morphology prior to film deposition for improved light conversion efficiency in scalable OSCs. The demonstrated ability to arrest VPS during the early stages can be applied in other industries and will especially afford control over the morphology of porous materials for applications ranging from membrane filtration to plastic foam manufacturing.

■ EXPERIMENTAL SECTION

Materials. Two different types of P3HT were used as received from Rieke Metals (Lincoln, NE), regionegular-P3HT (RR-P3HT) with $M_{\rm W}$ =50–70 kDa and regionegularity = 91%, and $M_{\rm W}$ = 70–90 kDa regionandom-P3HT (Rra-P3HT). PCBM was used as received from Solarmer Energy Inc. (Irwindale, CA). o-DCB was used as received from Sigma-Aldrich.

Sample Preparation. Solutions of P3HT were prepared by dissolving P3HT in *o*-DCB at 500 rpm and 60 °C on a magnetic stirrer hot plate overnight. Total P3HT concentrations were varied between 12.5, 25, 37.5, and 50 mg/mL. Solutions of blends of RR-P3HT and Rra-P3HT were prepared by weight ratios of 1:1 or 2:1.

Small-Amplitude Oscillatory Shearing. An Advanced Rheometric Expansion System (ARES) rheometer available from TA Instruments of New Castle, DE, was used in conjunction with a force rebalance transducer 0.2K-FRTN1 and stainless steel parallel disks with 8 and 25 mm diameters for small-amplitude oscillatory shearing experiments. The torque accuracy of the transducer is ± 0.02 g cm. The actuator of the ARES is a DC servo motor with a shaft supported by an air bearing with an angular displacement range of 5×10^{-6} to 0.5 rad, and an angular frequency range of 1×10^{-5} to 100 rad/s. It has an angular velocity range of 1×10^{-6} to 200 rad/s. As shown in Figure S2, the characterization involves a top disk attached to the upper fixture, which was connected to the torque and normal force transducers, and the bottom disk was attached to the bottom fixture of the rheometer, which was coupled to the motor. The rheometer was equipped with an environmental control chamber, which can operate from -70 to 600 °C with a ramp rate from 0.1 to 50 °C/min.

During oscillatory shearing, the shear strain, γ , varies sinusoidally with time, t, at a frequency of ω , i.e., $\gamma(t) = \gamma^0 \sin(\omega t)$, where γ^0 is the strain amplitude. The shear stress, $\tau(t)$, response of the fluid to the imposed oscillatory deformation consists of two contributions associated with the energy stored as elastic energy and energy dissipated as heat, i.e., $\tau(t) = G'(\omega)\gamma^0 \sin(\omega t) + G''(\omega)\gamma^0 \cos(\omega t)$. The

storage modulus, $G'(\omega)$, and the loss modulus, $G''(\omega)$, also define the magnitude of complex viscosity, $|\eta^*| = \sqrt{((G'/\omega)^2 + (G''/\omega)^2)}$, and $\delta = G''/G'$. In the linear viscoelastic region, all dynamic properties are independent of the strain amplitude, γ^0 . The samples were not presheared prior to thermal treatment and rheological characterization based on the understanding that, under certain conditions, strong structuring effects can be introduced via such preshearing to bias the subsequent characterizations of various rheological material functions. 10

Solutions were stirred on a hot plate at 60 $^{\circ}\text{C}$ prior to loading into the gap between two parallel disks. The temperature was decreased to the targeted subambient temperatures, -5, -10, and -15 °C, within 1 min after loading the solution in between parallel disks at room temperature. A thin layer of Fomblin oil was applied onto the free surface of the sandwiched sample to avoid solvent loss. 11 For each test, a fresh sample was loaded onto the rheometer to avoid any thermal and preshearing effects, unless indicated specifically. Special care was taken to probe the wall slip effect. Consistent with the exploration of the wall slip behavior of various complex fluids, including viscoplastic microgels and suspensions, 12-14 this was carried out by systematically varying the surface to volume ratios via changes in the testing gap between 0.5, 0.75, and 1 mm. 15 In order to characterize the sol-gel transition kinetics, the oscillatory shear data were collected first as a function of time at constant γ^0 and ω . The time sweep tests were stopped upon recording of ultimate plateau values of G' and G'' that were sustained for at least 10 min. This indicates that the gel that was formed had achieved a steady-state structure, and that the solvent loss was negligible. Upon reaching the plateau region, the dynamic properties, G' and G'', were collected as a function of frequency at a constant γ^0 within the linear viscoelastic region. Furthermore, temperature ramp tests were carried out to collect oscillatory shear data as a function of temperature at constant γ^0 and ω .

Cryo-Scanning Electron Microscopy (Cryo-SEM). Two microliter solutions were kept in aluminum sample holders, cooled to -5 or -15 °C, and held at these temperatures for 30 min to induce gelation following the collection of dynamic properties as a function of time. The gelled samples were then soaked in a liquid nitrogen bath at -199 °C to retain the microstructures during transfer for cryo-SEM imaging. The samples were then placed into a humidity-free cryotransfer system (Leica EM VCT100) before SEM imaging. In order to reveal the P3HT gel structure, solvent sublimation was carried out at -80 °C under a vacuum of 10^{-7} mbar for 10 min to remove the solvent and any condensed ice on the sample surfaces. The samples were then cooled down to -130 °C again for SEM imaging. SEM was carried out using a Zeiss Auriga Dual-Beam FIB-SEM (Carl Zeiss Microscopy) at an accelerating voltage of 5 kV using an Everhart—Thornley secondary electron detector.

Confocal Laser Scanning Microscopy (CLSM). A Nikon Ti-E inverted microscope, along with a C1 CLSM system, was used to characterize the morphological development of P3HT solutions during cooling. The solution was encapsulated inside a rectangular glass chamber with a wall thickness of 200 $\mu \rm m$, with another glass chamber filled with dry air attached below as a heat insulation layer. A Thermo Scientific NESLAB RTE 7 fluid bath was employed to control the temperature. Nitrogen gas was continuously purging the outer surface of the glass chamber to avoid water condensation under subambient temperatures. Heat flux sensors and thermocouples were employed to determine the true temperature distribution within the sample (refer to Figure S1 for a schematic of the setup and temperature distribution). P3HT was excited at a wavelength of 488 nm, and the emitted signal at a wavelength of 590 \pm 30 nm was collected.

Solar Cell Device Fabrication and Characterization. Patterned ITO-coated glass substrates (15 Ω sq⁻¹, Xinyang Technology Co.) were cleaned by sonication with acetone, deionized water, and isopropanol, sequentially, for 10 min each, followed by a 15 min O₂ plasma treatment. The 80-nm layers of PEDOT:PSS (Clevios F HC, Heraeus) were spin coated onto cleaned ITO substrates at

5000 rpm for 90 s and then annealed at 150 °C for 30 min in air. RRP3HT/PCBM solutions that had been cooled to -5 °C for various durations of time were then deposited on top of the PEDOT:PSS layers by blade coating. The devices were then transferred into a nitrogen glovebox for thermal annealing at 150 °C for 30 min. Finally, 1-nm LiF and 100-nm Al electrodes were deposited on top of the photoactive layers with a thermal evaporator (Covap, Angstrom Engineering Inc.) through a shadow mask. The device area was defined to be 0.046 cm². Current density versus voltage curves were collected in a N_2 atmosphere using a Keithley 2636B sourcemeter under simulated AM 1.5G irradiation (100 mW cm $^{-2}$). The intensity of the xenon arc lamp-based simulator (Model 11002, Abet Technologies Inc.) was calibrated using a monocrystalline Si reference cell.

RESULTS AND DISCUSSION

RR-P3HT, the most intensely studied semiconducting polymer for OSCs, 16 is well-known to form colloidal particles in solution via crystallization in a wide variety of solvents, giving rise to elastic behavior, i.e., gelation. ^{17–20} In the first study of the gelation of RR-P3HT solutions dissolved in xylene, a poor solvent for RR-P3HT, a two-step gelation mechanism involving a coil-to-rod transition followed by crystallization of the rods was proposed.²¹ Subsequent rheological and absorption measurements supported this mechanism of RR-P3HT aggregation via $\pi - \pi$ interactions, followed by physical linking of the aggregates to form a gel network.²² A similar pathway was observed for RR-P3HT dissolved in p-xylene, toluene, and benzene, using a combination of rheology and electrical conductivity characterization to determine the extent of percolation. 11 Small-angle X-ray scattering experiments of RR-P3HT/xylene gels later revealed the existence of RR-P3HT nanowhiskers.²³ These nanowhiskers were found to be only semicrystalline, likely due to restrictions imposed by extensive interchain interactions. Rheological tests to measure gel strength revealed that the gelation process can be inhibited by the presence of phenyl-C₆₁-butyric acid methyl ester (PCBM), a common electron acceptor codeposited with RR-P3HT to form photoactive layers.²

In addition to slow gelation at room temperature over a period of days, cooling RR-P3HT solutions can induce aggregation by lowering the solubility of RR-P3HT in the solvent. To monitor the cooling-induced gelation of RR-P3HT solutions in o-DCB, we performed a series of smallamplitude oscillatory shear tests as a function of P3HT concentration, time, frequency, and temperature. Figure 1a displays the storage modulus, G', of RR-P3HT solutions cooled to −5 °C from room temperature within 30 s after the environmental chamber was closed, and temperature control was switched on. Subsequently the temperature was kept constant at -5 °C for the characterization of the dynamic properties as a function of time. In addition to the control and monitoring of the tool temperature, the true temperature of the sample was independently verified using a thermocouple inserted into the sample. The experiments were carried out at RR-P3HT concentrations of 12.5, 25, and 50 mg/mL. Linear viscoelastic moduli were collected as a function of time at -5°C with a strain amplitude, γ^0 , and frequency, ω , of 1% and 1 rad/s, respectively.

As displayed in Figure 1a, the storage modulus, G', values of all three solutions increased monotonically with time at -5 °C. The rate of increase of G', i.e., dG'/dt, decreased with increasing time until G' reached a plateau. The plateau values reached, denoted as G'_{max} depended on the concentration of

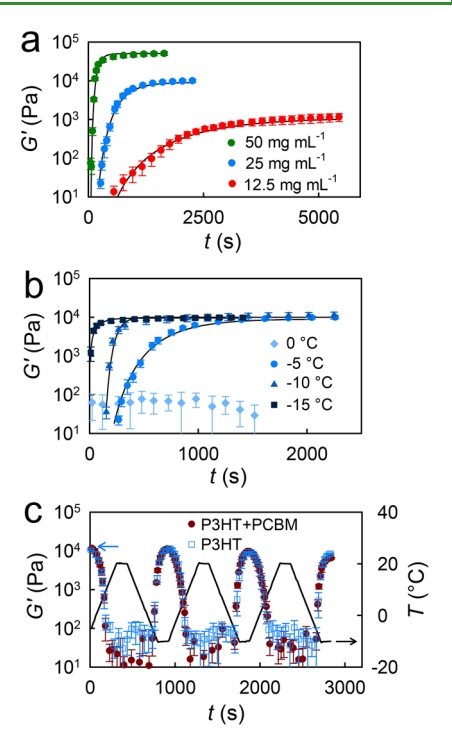


Figure 1. (a) Storage modulus, G', versus time, t, of RR-P3HT solutions in o-DCB with concentrations of 12.5, 25, and 50 mg/mL at -5 °C. Lines are provided to guide the eye. (b) Storage modulus, G', versus time, t, of 25 mg/mL RR-P3HT solutions cooled to 0, -5, -10, and -15 °C. (c) G' of a precooled 25 mg/mL RR-P3HT with and without 25 mg/mL PCBM versus t during temperature cycling between -10 and 20 °C. In all experiments, the frequency and the strain amplitude were kept constant at 1 rad/s and 1%, respectively.

the RR-P3HT, with the value of $G'_{\rm max}$ increasing from 1 to 50 kPa as the RR-P3HT concentration in o-DCB was increased from 12.5 to 50 mg/mL. The loss moduli, G'', values collected as a function of time for all three concentrations of the solutions were negligible in comparison to the values of G'; i.e., the G'' values were only in the 10–1000 Pa range, at least 50 times smaller than the corresponding storage moduli at the same frequency and strain amplitude applied.

The frequency scans carried out after reaching G'_{max} within the linear viscoelastic region (Figure S3) revealed that the dynamic properties remain independent of the frequency once G'_{max} is reached (Figure S4). Thus, for all concentrations of RR-P3HT, G' values were constant at their respective G'_{max} values over a frequency range of 0.1-100 rad/s. The observations that G' and G'' are independent of frequency and that the value of tan $\delta = G''/G'$ is smaller than 0.1 in this range, i.e., $G'(\omega)\gg G''(\omega)$, are both hallmarks of gel-like behavior. The observed $G'(\omega)\gg G''(\omega)$ behavior indicates that relatively long relaxation times prevail, i.e., a precursor of solid-like behavior (Figure S4). The timedependent increase of the storage modulus describes the transformation of the RR-P3HT solution from a fluid to a gel, i.e., "gelation process for RR-P3HT". The ultimate value of the storage modulus that is attained, i.e., G'_{max} , is indicative of the strength of the gel.

In addition to affecting the gel strength, the concentration of RR-P3HT in solution was also found to affect the rate of gelation represented by dG'/dt. The rate of gelation increased with an increasing concentration of RR-P3HT. A characteristic gelation time, $t_{\mathcal{O}}$ was defined as the time at which the

maximum value of dG'(t)/dt normalized to $G'_{\rm max}$ was observed (Figure S5). With increasing RR-P3HT concentration from 12.5 to 50 mg/mL, $t_{\rm c}$ decreased from 2000 to 200 s, indicating a faster rate of gelation with increasing RR-P3HT concentration.

To probe the effect of the temperature on the development of the rate of gelation and gel strength, time sweeps were carried out on fresh solutions of 25 mg/mL RR-P3HT in o-DCB, which were cooled to temperatures in the range of 0 to −15 °C. All of the targeted temperatures were reached within 30 s after the environmental chamber was closed, and temperature control was switched on. As displayed in Figure 1b, G' of a 25 mg/mL RR-P3HT solution in o-DCB cooled to 0 °C remained constant, exhibiting a relatively small value for at least 1500 s. For 25 mg/mL RR-P3HT solutions cooled to -5 to -15 °C, on the other hand, a dramatic increase in G'from negligible values to a $G'_{\text{max}} = 10^4 \text{ Pa}$ was observed. G'_{max} is a direct measure to the number of cross-links in the gel. Its temperature independence indicates that the number of crosslinks formed by the gel is not kinetically limited (Figure S6). Given sufficient time to gel, the maximum number of possible cross-links, as determined by the polymer chain concentration, is achieved for all quenching temperatures.³² However, the characteristic gelation time, t_c decreased from 800 to 250 s as the temperature decreased from -5 to -15 °C, reflecting a significant increase of the rate of gelation with decreasing temperature (Figure S7). These observations on the dependencies of the dynamic properties on time and temperature are in line with a recent investigation of fraction of aggregated RR-P3HT in o-DCB between 0 and -5 °C using Raman spectroscopy.³³ These experiments have revealed the occurrence of a sharp transition from RR-P3HT unimers to RR-P3HT aggregates. This transition was attributed to the solution concentration coinciding with the solubility limit of RR-P3HT, which decreases with decreasing temperature.34

We also performed oscillatory shear experiments during temperature cycling between 20 and −10 °C on 25 mg/mL RR-P3HT solutions in o-DCB that were precooled to −5 °C for 30 min to examine the reversibility of the observed sol-gel transition. Figure 1c displays the temperature and storage modulus of the solution versus time. G' tracked closely to the temperature profile during cycling, displaying values of <100 and 10⁴ Pa at 20 and −10 °C, respectively. Interestingly, the characteristic time for gelation during temperature cycling was 5 times faster compared to the initial gelation rate of a fresh RR-P3HT solution cooled from room temperature. This observation suggests that some "memory" of the gel structure persists during heating to 20 °C, even though the solution behavior approaches the behavior of a viscous fluid at 20 °C. Oh and co-workers studied the growth of P3HT nanofibrils in solutions by a cycle of cooling and heating, concluding that such "memory" effect is due to the crystallinity hysteresis upon temperature cycling.²⁷ Newbloom and co-workers likewise found persistence of the P3HT fiber network after dissolution of the gel phase.35

For bulk-heterojunction OSC applications, RR-P3HT is most commonly codissolved in solution with PCBM, which is then spun cast onto device platforms to form the photoactive layer. The presence of PCBM has been found to significantly disrupt the crystallization of RR-P3HT when the two compounds are codeposited in this manner. ^{36,37} To examine the effect of PCBM on the thermoreversible gelation of RR-P3HT, the linear viscoelastic material functions of a solution

comprising 25 mg/mL of PCBM codissolved with 25 mg/mL RR-P3HT in o-DCB were characterized. Surprisingly, the presence of PCBM did not significantly alter the thermoreversible gelation behavior of RR-P3HT, with no observable change in the characteristic gelation time or gel strength (Figure 1c). This finding contradicts a previous report which suggested that both the rate of gelation and steady-state gel strength of 80 mg/mL RR-P3HT dissolved in o-DCB at 5 °C significantly decreased in the presence of PCBM.²⁴ We hypothesize that this discrepancy is due to differences in the gelation mechanism in different temperature regimes. RR-P3HT solutions form gels at room temperature over a period of days via the crystallization-driven self-assembly of RR-P3HT chains into nanowhiskers, which then interconnect to form a network. 22,23,38-40 In contrast, we observe gelation to occur on the order of minutes in RR-P3HT solutions cooled rapidly to subambient temperatures, with or without PCBM, which likely proceeds via an alternate gelation pathway. Interestingly, when PCBM is replaced with small-molecule triisopropylsilylethynyl pentacene (TIPS-PEN), RR-P3HT gelation is significantly suppressed in the temperature and time ranges examined (Figure S8). In line with previous findings that the miscibility of the semiconducting polymer and small molecule play a critical role in morphological evolution during film deposition, 41-43 our observations indicate that TIPS-PEN, with planar aromatic cores that can interact with those of semirigid RR-P3HT and increased solubility in o-DCB compared to PCBM, 44,45 disrupts interchain RR-P3HT crystallization.

To examine the role of crystallization on rapid RR-P3HT gelation upon cooling, we examined the behavior of solutions comprising noncrystallizing Rra-P3HT of similar molecular weight to that of the RR-P3HT used in these studies. Time sweeps of 25 mg/mL Rra-P3HT solutions in *o*-DCB revealed that Rra-P3HT does not form a gel upon being cooled to -5 °C. As displayed in Figure 2a, the storage modulus of the solution comprising pure Rra-P3HT at a concentration of 25 mg/mL remained below 10 Pa upon being cooled. The observation that noncrystallizing Rra-P3HT does not form a

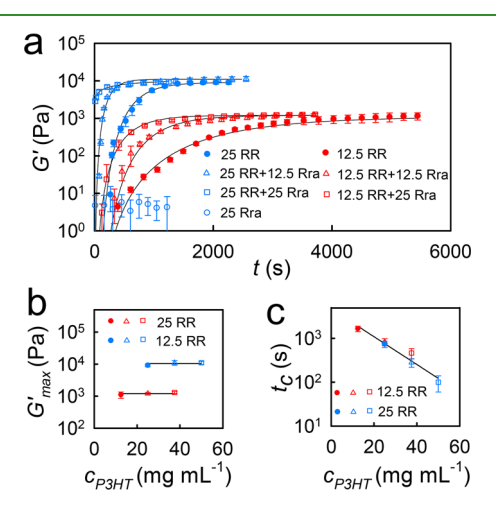


Figure 2. (a) G' versus time of solutions comprising blends of RR-and Rra-P3HT in o-DCB with concentrations of 12.5 and 25 mg/mL, cooled from room temperature to -5 °C. (b) Steady-state storage modulus, G'_{max} of the solutions versus the total concentration of P3HT. (c) Characteristic gelation time of the solutions, t_c , versus the total concentration of P3HT.

gel thus indicates that intrachain crystallization, not chain entanglements, form the junctions in RR-P3HT gels.

In contrast to pure Rra-P3HT solutions, solutions comprising blends of RR-P3HT and Rra-P3HT with concentration ratios from 1:0.5 to 1:2 and total P3HT concentrations up to 50 mg/mL in o-DCB still exhibited gel formation upon being cooled to -5 °C. Surprisingly, G'_{max} was found to depend solely on the concentration of RR-P3HT and was independent of the Rra-P3HT concentration in the blended solutions (Figure 2b). These results indicate that the presence of Rra-P3HT does not disrupt the crystallization of RR-P3HT in solution, nor does its presence contribute to the gel strength despite an increase in the total polymer content at the concentration and temperature ranges of our investigation.

However, although the gel strength is not affected, the rate of gelation was found to strongly depend on the total P3HT content, as displayed in Figure 2c. The characteristic gelation time, to decreased significantly from 2000 to 100 s as the P3HT content (RR- plus Rra-P3HT) increased from 12.5 to 50 mg/mL, independent of the specific ratio of Rra-P3HT to RR-P3HT. The presence of Rra-P3HT thus accelerates the rate of gelation, which is attributed to the network formation of RR-P3HT. Previous findings in the literature are in disagreement on the ability of Rra-P3HT to disrupt the crystallization of RR-P3HT in blends. For example, a two order-of-magnitude decrease in hole mobility upon addition of Rra-P3HT to RR-P3HT films acting as active layers in field-effect transistors was attributed to decreased RR-P3HT crystallization. 46 On the other hand, unfavorable interactions between Rra-P3HT and RR-P3HT were found to lead to vertical phase separation between the two polymers in transistor active layers. 47 Devices comprising these vertically segregated blends displayed no significant decrease in performance compared to those comprising pure RR-P3HT in the active layer. To the best of our knowledge, the observed acceleration of RR-P3HT crystallization in the presence of Rra-P3HT has not been reported earlier.

Combined, our observations that the presence of Rra-P3HT (1) does not affect the final gel strength and (2) increases the rate of gelation provide direct evidence for a two-step gelation mechanism in these polymer solutions. In agreement with our finding that the presence of PCBM does not affect the kinetics or extent of RR-P3HT gelation, we hypothesize that cooling the solutions below the solubility limit of RR-P3HT first induces phase separation of RR-P3HT into polymer-rich and polymer-poor domains within the solution. This phase separation is followed by interchain crystallization of the RR-P3HT phase into nanofibrils that form the gel network to span the volume. In the absence of phase separation, we would expect the presence of Rra-P3HT chains to impede RR-P3HT crystallization. The characteristic time for gelation, t_c , is thus a measure of the rate of phase separation to form RR-P3HT-rich domains, and G'_{max} is a measure of the number density of crystalline affine junction points, i.e., the physical cross-links, formed in the gel network.

Direct high-resolution imaging of P3HT gels to confirm the network morphology is exceedingly difficult because of the presence of organic solvents that are generally incompatible with vacuum-based imaging techniques. Furthermore, processing methods that rely on the removal of the solvent for subsequent imaging, such as heating or slow solvent evaporation, unavoidably alter the gel morphology. Using a novel cryogen-based imaging method pioneered by the Libera

group, ⁴⁸ we collected high-resolution SEM images of cooled P3HT gels in partially solvated environments to capture morphological features on the nanometer length scale. As detailed in the Experimental Section, 25 mg/mL P3HT solutions were cooled to -5 °C for 30 min to induce gelation. The gels were then flash-frozen in liquid nitrogen, followed by partial solvent sublimation at a pressure of 1×10^{-7} mbar and temperature of -80 °C for 10 min. Longer sublimation times to completely remove the solvent led to the collapse of the gel structure, as confirmed by SEM imaging (Figure S9).

Figure 3a displays an SEM image of a partially solvated RR-P3HT gel. As observed in the figure, a nanofibrous

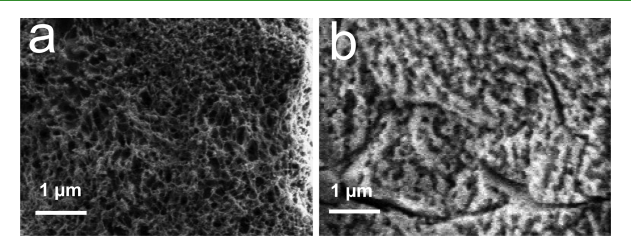


Figure 3. Cryogen-based SEM images of partially desolvated samples comprising (a) RR-P3HT and (b) Rra-P3HT.

interconnected network with pore sizes on the tens to hundreds of nanometers length scale is observed. This morphology is consistent with our proposed mechanism of interchain polymer crystallization during cooling and is reminiscent of structures observed in freeze-dried P3HT gel samples. We observe fiber diameters that are comparable to those previously reported. For reference, similarly processed samples comprising Rra-P3HT appeared glassy and did not display a fibrous network due to the inability of Rra-P3HT to crystallize (Figure 3b).

To monitor morphological development of P3HT solutions in real-time during cooling, we exploited the photoluminescence (PL) properties of P3HT. When excited at a wavelength of 488 nm, P3HT emits a PL signal between 500 and 700 nm, with a maximum PL signal around 570 nm. 52 We employed temperature-variable CLSM to observe the gelation process and gain insight into the gelation mechanism in our system. The PL signal of RR- and Rra-P3HT solutions in o-DCB at room temperature and cooled to -5 °C under 488 nm laser excitation was mapped. As displayed in Figure 4a, the fluorescence signal collected on a 25 mg/mL RR-P3HT solution in o-DCB at room temperature was spatially uniform, indicating that the polymer was well-dissolved in the solvent. Upon being cooled to −5 °C, dark "holes" with diameters ranging from 1 to 5 μ m in the fluorescence micrograph appeared (Figure 4b). These solvent-rich holes, a hallmark of the early stages of viscoelastic phase separation, form due to dynamic asymmetry between the fast-moving solvent molecules and slow-moving polymer chains. The natural progression of viscoelastic phase separation is for the solvent holes to grow and coalesce, eventually forming the majority phase. Interestingly, the holes in cooled RR-P3HT solutions persisted until the solutions were reheated to room temperature. Our rheological and fluorescence microscopy experiments indicate that these porous gels are stable, with no change in gel properties or morphology after 20 min. We thus hypothesize that interchain RR-P3HT crystallization arrests viscoelastic phase separation in the early stages of solvent hole formation, as illustrated in Figure 4c.

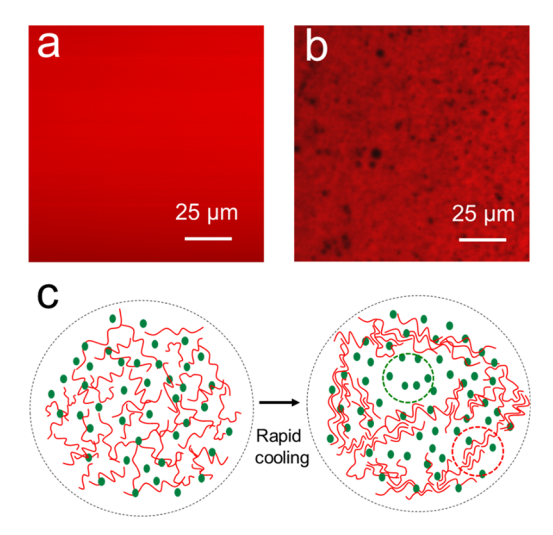


Figure 4. CLSM images of a 25 mg/mL RR-P3HT solution in σ -DCB at (a) 20 and (b) at -5 °C. (c) Illustration of the RR-P3HT solution before and after cooling-induced viscoelastic phase separation. A solvent hole and interchain crystal are highlighted by green- and red-dashed circles, respectively.

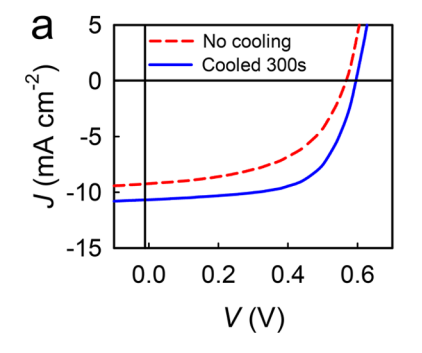
The formation of porous "crystal gels" via crystallizationarrested viscoelastic phase separation has previously been observed in supercooled colloidal suspensions. 8,53 Monitoring the process at the single-particle level, Tanaka and co-workers recently proposed a set of requirements for observing this phenomenon, including a driving force for phase separation below the melting point of the colloidal crystal phase and a low energy barrier to crystallization.8 In our system, we induce phase separation by rapidly cooling the solution to lower the solubility of P3HT in the solvent. Once the solubility of P3HT in o-DCB falls below the solution concentration, phase separation is induced. Because o-DCB is a relatively good solvent for P3HT, 45 we expect the chains to adopt large endto-end distances, which in turn facilitates interchain crystallization. Given the ability to tune the driving force for interchain crystallization by varying the degree of regioregularity 54,55 and the solvent quality, 56-58 this model system will open new avenues to explore factors governing crystallizationarrested viscoelastic phase separation in dilute polymer solutions.

Network structures have critical applications in fields ranging from membrane filtration to food processing.¹ In the field of solution-processable OSCs, the reproducible formation of

interconnected, crystalline networks of semiconducting polymers can significantly affect device performance by providing a continuous, high-mobility network for efficient charge transport and large interfacial area with the electron-accepting (or donating) phase for exciton dissociation. Critically, controlling the solution structure prior to deposition will enable the continuous processing of high-performance OSC photoactive layers in a scalable manner.

As a demonstration of morphological control in OSC photoactive layers via solution-phase gelation to improve OSC device performance, we fabricated OSCs comprising doctorbladed RR-P3HT/PCBM solutions cooled to -5 °C for varying durations of time (see Experimental Section for fabrication details). Figure 5a displays characteristic J-V curves for OSCs comprising RR-P3HT/PCBM photoactive layers deposited without solution cooling and with 300 s of solution cooling to -5 °C. The efficiency of the OSC comprising a photoactive layer deposited from a precooled solution was found to be higher compared to that of the reference device, resulting in an overall improvement in the power conversion efficiency from 2.7 ± 0.2 to $3.9 \pm 0.2\%$. Specifically, the short circuit current density, J_{sc} , was found to increase from 9.1 to 10.7 mA/cm² upon rapid solution cooling prior to film deposition, corresponding to improved charge mobility through the active layer. We attribute this improvement to a more interconnected, crystalline polymer network that forms upon rapid cooling compared to uncooled samples. The open circuit voltage, $V_{\rm OC}$, also increased from 0.56 to 0.60 V. The $V_{\rm OC}$, while ultimately limited by the relative band gaps of the electron donor and acceptor, is also affected by the active layer morphology. ^{59,60} In this case, we expect the improved VPS-induced morphology in cooled active layers to decrease nonradiative recombination losses during light conversion, leading to an increase in the $V_{\rm OC}$ compared to reference cells. The efficiencies of these devices were found to decrease by 50% after three months of storage in a nitrogen environment, similar to other reports in the literature. 61 Improving the shelf life of organic solar cells, for example, via electrode engineering and encapsulation, 62 is an area of intense investigation and will be explored in future studies.

Figure 5b displays the power conversion efficiency, PCE, as a function of the solution cooling duration at -5 °C prior to blade coating. Interestingly, the maximum efficiency is observed for a cooling duration of 300 s. Upon longer cooling times, the efficiency decreased. On the basis of our rheological measurements displayed in Figure 1, gel formation completes by ~1000 s for solutions comprising 25 mg/mL RR-P3HT.



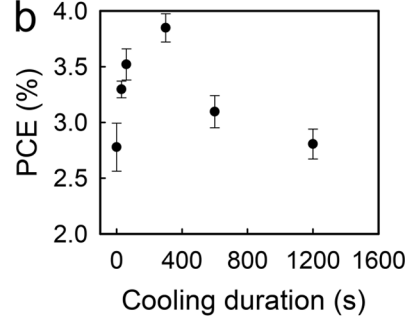


Figure 5. (a) Representative *J*−*V* curves of OSCs comprising photoactive layers blade-coated from an uncooled solution and a solution cooled to −5 °C for 300 s. (b) PCE of OSCs versus the cooling duration of the RR-P3HT/PCBM solution prior to blade coating. Error bars represent the standard deviation in efficiencies for three devices.

We speculate that this decrease in efficiency is related to the extent of phase separation between RR-P3HT and PCBM at different points in the cooling process. As a small molecule, PCBM is not expected to display dynamic asymmetry with the solvent. PCBM is thus present within the solvent holes that form during viscoelastic phase separation between the solvent and RR-P3HT. As these holes grow, likewise do the PCBMrich domains that form upon solvent removal during blade coating. It is well-established, that while some degree of phase separation between RR-P3HT and PCBM improves device efficiency by increasing the number of continuous pathways in the RR-P3HT and PCBM phases to the anode and cathode, respectively, extensive phase separation results in a decrease in interfacial area for exciton dissociation and thus lower device efficiency. 63-65 In our proposed method, we can control the extent of phase separation between RR-P3HT and PCBM by stopping the gelation process at different time points.

CONCLUSION

Viscoelastic phase separation, a phenomenon unique to polymer and colloidal systems displaying dynamic asymmetry between components, is a powerful thermodynamic process to form interconnected network structures. As revealed by a combination of rheological characterization and temperaturedependent advanced microscopy methods, we have discovered a pathway to arrest viscoelastic phase separation in RR-P3HT solutions at early stages via interchain crystallization in order to form semicrystalline gel networks with hierarchical porosity. RR-P3HT network strength was insensitive to the presence of both PCBM and regiorandom P3HT, as monitored by oscillatory shear measurements. The ability to form the porous network in the presence of a second component will have a broad impact in a variety of fields, including optoelectronics. By affording continuous pathways for charge transport and large interfacial area with the electron-accepting PCBM phase, the presence of these RR-P3HT networks in the photoactive layers of OSCs was demonstrated to enhance solar conversion efficiency from 2.7 ± 0.2 to $3.9 \pm 0.2\%$. Significantly, these networks were formed in solution prior to photoactive layer deposition in a highly reproducible manner. Crystallizationarrested viscoelastic phase separation thus presents a promising strategy to achieve optimal photoactive layer morphologies by controlling the structure of polymer-small molecule solutions. Furthermore, this processing method is compatible with largescale manufacturing methods to continuously process OSC photoactive layers from solution, which will be critical in advancing this technology toward industrial acceptance.

ASSOCIATED CONTENT

S Supporting Information

The Supporting Information is available free of charge on the ACS Publications website at DOI: 10.1021/acsapm.8b00195.

Methods, design, and supporting figures of the characterization data (PDF)

AUTHOR INFORMATION

Corresponding Author

*E-mail: stephanie.lee@stevens.edu.

ORCID 6

Dilhan M. Kalyon: 0000-0003-2066-0359 Stephanie S. Lee: 0000-0003-0964-6353

Notes

The authors declare no competing financial interest.

ACKNOWLEDGMENTS

This material is based upon work supported by the National Science Foundation under Grant 1635284. The authors are also grateful for additional financial support received from PSEG to advance energy innovation at Stevens. Portions of the research used microscopy resources within the Laboratory for Multiscale Imaging at Stevens Institute of Technology. We thank Prof. M. Libera and Dr. T. Chou for their help with microscopy experiments.

REFERENCES

- (1) Tanaka, H. Formation of Network and Cellular Structures by Viscoelastic Phase Separation. *Adv. Mater.* **2009**, 21, 1872–1880.
- (2) Tanaka, H. Unusual Phase Separation in a Polymer Solution Caused by Asymmetric Molecular Dynamics. *Phys. Rev. Lett.* **1993**, *71*, 3158–3161.
- (3) Tanaka, H. Viscoelastic Phase Separation. J. Phys.: Condens. Matter 2000, 12, R207-R264.
- (4) Tanaka, H. Appearance of a Moving Droplet Phase and Unusual Networklike or Spongelike Patterns in a Phase-Separating Polymer Solution with a Double-Well-Shaped Phase Diagram. *Macromolecules* **1992**, 25, 6377–6380.
- (5) Mezzenga, R.; Schurtenberger, P.; Burbidge, A.; Michel, M. Understanding Foods as Soft Materials. *Nat. Mater.* **2005**, *4*, 729–740.
- (6) She, H.; Xiao, X.; Liu, R. Preparation and Characterization of Polycaprolactone-Chitosan Composites for Tissue Engineering Applications. *J. Mater. Sci.* **2007**, *42*, 8113–8119.
- (7) Tanaka, H.; Nishikawa, Y. Viscoelastic Phase Separation of Protein Solutions. *Phys. Rev. Lett.* **2005**, *95*, 078103.
- (8) Tsurusawa, H.; Russo, J.; Leocmach, M.; Tanaka, H. Formation of Porous Crystals via Viscoelastic Phase Separation. *Nat. Mater.* **2017**, *16*, 1022–1028.
- (9) Jackson, N. E.; Savoie, B. M.; Marks, T. J.; Chen, L. X.; Ratner, M. A. The Next Breakthrough for Organic Photovoltaics? *J. Phys. Chem. Lett.* **2015**, *6*, 77–84.
- (10) Küçük, I.; Gevgilili, H.; Kalyon, D. M. Effects of Dispersion and Deformation Histories on Rheology of Semidilute and Concentrated Suspensions of Multiwalled Carbon Nanotubes. *J. Rheol.* **2013**, *57*, 1491–1514.
- (11) Newbloom, G. M.; Weigandt, K. M.; Pozzo, D. C. Electrical, Mechanical, and Structural Characterization of Self-Assembly in Poly (3-hexylthiophene) Organogel Networks. *Macromolecules* **2012**, *45*, 3452–3462.
- (12) Ortega-Avila, J. F.; Pérez-González, J.; Marín-Santibáñez, B. M.; Rodríguez-González, F.; Aktas, S.; Malik, M.; Kalyon, D. M. Axial Annular Flow of A Viscoplastic Microgel with Wall Slip. *J. Rheol.* **2016**, *60*, 503–515.
- (13) Medina-Bañuelos, E. F.; Marín-Santibáñez, B. M.; Pérez-González, J.; Malik, M.; Kalyon, D. M. Tangential Annular (Couette) Flow of A Viscoplastic Microgel with Wall Slip. *J. Rheol.* **2017**, *61*, 1007–1022
- (14) He, J.; Lee, S. S.; Kalyon, D. M. Shear Viscosity and Wall Slip Behavior of Dense Suspensions of Polydisperse Particles. *J. Rheol.* **2019**, *63*, 19–32.
- (15) Aktas, S.; Kalyon, D. M.; Marín-Santibáñez, B. M.; Pérez-González, J. Shear Viscosity and Wall Slip Behavior of a Viscoplastic Hydrogel. *J. Rheol.* **2014**, *58*, 513–535.
- (16) Dang, M. T.; Hirsch, L.; Wantz, G. P3HT: PCBM, Best Seller in Polymer Photovoltaic Research. Adv. Mater. 2011, 23, 3597–3602.
- (17) Newbloom, G. M.; Kim, F. S.; Jenekhe, S. A.; Pozzo, D. C. Mesoscale Morphology and Charge Transport in Colloidal Networks of Poly (3-hexylthiophene). *Macromolecules* **2011**, *44*, 3801–3809.

- (18) Huang, Y.; Cheng, H.; Han, C. C. Unimer–Aggregate Equilibrium to Large Scale Association of Regioregular Poly (3-hexylthiophene) in THF Solution. *Macromolecules* **2011**, *44*, 5020–5026
- (19) Huang, Y.; Cheng, H.; Han, C. C. Temperature Induced Structure Evolution of Regioregular Poly (3-hexylthiophene) in Dilute Solution and Its Influence on Thin Film Morphology. *Macromolecules* **2010**, 43, 10031–10037.
- (20) Yi, H.-L.; Hua, C.-C. Peculiar Aggregation Features in Poly(3-hexylthiophene)/Chlorobenzene Solutions. *Macromolecules* **2019**, *52*, 332–340.
- (21) Malik, S.; Jana, T.; Nandi, A. K. Thermoreversible Gelation of Regioregular Poly (3-hexylthiophene) in Xylene. *Macromolecules* **2001**, *34*, 275–282.
- (22) Koppe, M.; Brabec, C. J.; Heiml, S.; Schausberger, A.; Duffy, W.; Heeney, M.; McCulloch, I. Influence of Molecular Weight Distribution on the Gelation of P3HT and Its Impact on The Photovoltaic Performance. *Macromolecules* **2009**, 42, 4661–4666.
- (23) Chen, C.-Y.; Chan, S.-H.; Li, J.-Y.; Wu, K.-H.; Chen, H.-L.; Chen, J.-H.; Huang, W.-Y.; Chen, S.-A. Formation and Thermally-Induced Disruption of Nanowhiskers in Poly (3-hexylthiophene)/xylene Gel Studied by Small-Angle X-ray Scattering. *Macromolecules* 2010, 43, 7305–7311.
- (24) Sobkowicz, M. J.; Jones, R. L.; Kline, R. J.; DeLongchamp, D. M. Effect of Fullerenes on Crystallization-Induced Aggregation in Polymer Photovoltaics Casting Solutions. *Macromolecules* **2012**, 45, 1046–1055.
- (25) Park, Y. D.; Lee, H. S.; Choi, Y. J.; Kwak, D.; Cho, J. H.; Lee, S.; Cho, K. Solubility-Induced Ordered Polythiophene Precursors for High-Performance Organic Thin-Film Transistors. *Adv. Funct. Mater.* **2009**, *19*, 1200–1206.
- (26) Dang, M. T.; Wantz, G.; Bejbouji, H.; Urien, M.; Dautel, O. J.; Vignau, L.; Hirsch, L. Polymeric Solar Cells Based on P3HT: PCBM: Role of the Casting Solvent. *Sol. Energy Mater. Sol. Cells* **2011**, 95, 3408–3418.
- (27) Oh, J. Y.; Shin, M.; Lee, T. I.; Jang, W. S.; Min, Y.; Myoung, J.-M.; Baik, H. K.; Jeong, U. Self-Seeded Growth of Poly (3-hexylthiophene)(P3HT) Nanofibrils by a Cycle of Cooling and Heating in Solutions. *Macromolecules* **2012**, *45*, 7504–7513.
- (28) Berson, S.; De Bettignies, R.; Bailly, S.; Guillerez, S. Poly (3-hexylthiophene) Fibers for Photovoltaic Applications. *Adv. Funct. Mater.* **2007**, *17*, 1377–1384.
- (29) De Rosa, M.; Winter, H. The Effect of Entanglements on the Rheological Behavior of Polybutadiene Critical Gels. *Rheol. Acta* **1994**, 33, 220–237.
- (30) Winter, H. H.; Chambon, F. Analysis of Linear Viscoelasticity of a Crosslinking Polymer at the Gel Point. *J. Rheol.* **1986**, *30*, 367–382.
- (31) Vural, S.; Dikovics, K. B.; Kalyon, D. M. Cross-link Density, Viscoelasticity and Swelling of Hydrogels as Affected by Dispersion of Multi-Walled Carbon Nanotubes. *Soft Matter* **2010**, *6*, 3870–3875.
- (32) Weng, L.; Chen, X.; Chen, W. Rheological Characterization of in situ Crosslinkable Hydrogels Formulated from Oxidized Dextran and N-carboxyethyl Chitosan. *Biomacromolecules* **2007**, *8*, 1109–1115.
- (33) Lan, Y.-B.; Sher, P.-H.; Lee, C.-K.; Pao, C.-W.; Tsao, C.-S.; Huang, Y.-C.; Huang, P.-T.; Wu, C.-I.; Wang, J.-K. Revealing Ordered Polymer Packing during Freeze-Drying Fabrication of a Bulk Heterojunction Poly (3-hexylthiophene-2, 5-diyl):[6, 6]-Phenyl-C61-butyric Acid Methyl Ester Layer: In Situ Optical Spectroscopy, Molecular Dynamics Simulation, and X-ray Diffraction. *J. Phys. Chem. C* 2017, 121, 14826–14834.
- (34) Schmidt-Hansberg, B.; Sanyal, M.; Klein, M. F.; Pfaff, M.; Schnabel, N.; Jaiser, S.; Vorobiev, A.; Müller, E.; Colsmann, A.; Scharfer, P.; et al. Moving Through the Phase Diagram: Morphology Formation in Solution Cast Polymer–Fullerene Blend Films for Organic Solar Cells. *ACS Nano* **2011**, *5*, 8579–8590.
- (35) Newbloom, G. M.; Weigandt, K. M.; Pozzo, D. C. Structure and Property Development of Poly (3-hexylthiophene) Organogels

- Probed with Combined Rheology, Conductivity and Small Angle Neutron Scattering. *Soft Matter* **2012**, *8*, 8854–8864.
- (36) Treat, N. D.; Brady, M. A.; Smith, G.; Toney, M. F.; Kramer, E. J.; Hawker, C. J.; Chabinyc, M. L. Interdiffusion of PCBM and P3HT Reveals Miscibility in a Photovoltaically Active Blend. *Adv. Energy Mater.* **2011**, *1*, 82–89.
- (37) Kozub, D. R.; Vakhshouri, K.; Orme, L. M.; Wang, C.; Hexemer, A.; Gomez, E. D. Polymer Crystallization of Partially Miscible Polythiophene/Fullerene Mixtures Controls Morphology. *Macromolecules* **2011**, *44*, 5722–5726.
- (38) Huang, W.; Huang, P.; Han, Y.; Lee, C.; Hsieh, T.; Chang, M. Aggregation and Gelation Effects on The Performance of Poly (3-hexylthiophene)/Fullerene Solar Cells. *Macromolecules* **2008**, *41*, 7485–7489.
- (39) Xue, L.; Gao, X.; Zhao, K.; Liu, J.; Yu, X.; Han, Y. The Formation of Different Structures of Poly (3-hexylthiophene) Film on A Patterned Substrate by Dip Coating from Aged Solution. *Nanotechnology* **2010**, *21*, 145303–145312.
- (40) Bielecka, U.; Lutsyk, P.; Janus, K.; Sworakowski, J.; Bartkowiak, W. Effect of Solution Aging on Morphology and Electrical Characteristics of Regioregular P3HT FETs Fabricated by Spin Coating and Spray Coating. Org. Electron. 2011, 12, 1768–1776.
- (41) Ye, L.; Hu, H.; Ghasemi, M.; Wang, T.; Collins, B. A.; Kim, J.-H.; Jiang, K.; Carpenter, J. H.; Li, H.; Li, Z.; McAfee, T.; Zhao, J.; Chen, X.; Lai, J. L. Y.; Ma, T.; Bredas, J.-L.; Yan, H.; Ade, H. Quantitative Relations between Interaction Parameter, Miscibility and Function in Organic Solar Cells. *Nat. Mater.* 2018, *17*, 253–260.
- (42) Collins, B. A.; Gann, E.; Guignard, L.; He, X.; McNeill, C. R.; Ade, H. Molecular Miscibility of Polymer–Fullerene Blends. *J. Phys. Chem. Lett.* **2010**, *1*, 3160–3166.
- (43) Liu, Y.; Zhao, J.; Li, Z.; Mu, C.; Ma, W.; Hu, H.; Jiang, K.; Lin, H.; Ade, H.; Yan, H. Aggregation and Morphology Control Enables Multiple Cases of High-Efficiency Polymer Solar Cells. *Nat. Commun.* **2014**, *5*, 5293.
- (44) Payne, M. M.; Parkin, S. R.; Anthony, J. E.; Kuo, C.-C.; Jackson, T. N. Organic Field-Effect Transistors from Solution-Deposited Functionalized Acenes with Mobilities as High as 1 cm2/V·s. J. Am. Chem. Soc. 2005, 127, 4986–4987.
- (45) Machui, F.; Langner, S.; Zhu, X.; Abbott, S.; Brabec, C. J. Determination of the P3HT: PCBM Solubility Parameters via a Binary Solvent Gradient Method: Impact of Solubility on the Photovoltaic Performance. Sol. Energy Mater. Sol. Cells 2012, 100, 138–146
- (46) Nam, S.; Lee, S.; Lee, I.; Shin, M.; Kim, H.; Kim, Y. Nanomorphology-Driven Two-Stage Hole Mobility in Blend Films of Regioregular and Regiorandom Polythiophenes. *Nanoscale* **2011**, *3*, 4261–4269.
- (47) Chu, P. H.; Wang, G.; Fu, B.; Choi, D.; Park, J. O.; Srinivasarao, M.; Reichmanis, E. Synergistic Effect of Regioregular and Regiorandom Poly (3-hexylthiophene) Blends for High Performance Flexible Organic Field Effect Transistors. *Adv. Electron. Mater.* **2016**, 2, 1500384.
- (48) Liang, J.; Teng, F.; Chou, T.-M.; Libera, M. Measuring Microgel Swell Ratio by Cryo-SEM. *Polymer* **2017**, *116*, 1–4.
- (49) Huang, P. T.; Chang, Y. S.; Chou, C. W. Preparation of Porous Poly (3-hexylthiophene) by Freeze-Dry Method and Its Application to Organic Photovoltaics. *J. Appl. Polym. Sci.* **2011**, *122*, 233–240.
- (50) Liu, J.; Arif, M.; Zou, J.; Khondaker, S. I.; Zhai, L. Controlling Poly (3-hexylthiophene) Crystal Dimension: Nanowhiskers and Nanoribbons. *Macromolecules* **2009**, *42*, 9390–9393.
- (51) Ihn, K. J.; Moulton, J.; Smith, P. Whiskers of Poly (3-alkylthiophene) s. J. Polym. Sci., Part B: Polym. Phys. 1993, 31, 735–742.
- (52) Ferreira, B.; da Silva, P. F.; Seixas de Melo, J. S. r.; Pina, J. o.; Maçanita, A. n. Excited-State Dynamics and Self-Organization of Poly (3-hexylthiophene)(P3HT) in Solution and Thin Films. *J. Phys. Chem. B* **2012**, *116*, 2347–2355.
- (53) Sabin, J.; Bailey, A. E.; Espinosa, G.; Frisken, B. J. Crystal-Arrested Phase Separation. *Phys. Rev. Lett.* **2012**, *109*, 195701.

- (54) Kim, Y.; Cook, S.; Tuladhar, S. M.; Choulis, S. A.; Nelson, J.; Durrant, J. R.; Bradley, D. D.; Giles, M.; McCulloch, I.; Ha, C.-S.; Ree, M. A Strong Regioregularity Effect in Self-Organizing Conjugated Polymer Films and High-Efficiency Polythiophene: Fullerene Solar Cells. *Nat. Mater.* **2006**, *5*, 197–203.
- (55) Woo, C. H.; Thompson, B. C.; Kim, B. J.; Toney, M. F.; Fréchet, J. M. The Influence of Poly (3-hexylthiophene) Regioregularity on Fullerene-Composite Solar Cell Performance. *J. Am. Chem. Soc.* **2008**, *130*, 16324–16329.
- (56) Yang, H.; LeFevre, S. W.; Ryu, C. Y.; Bao, Z. Solubility-Driven Thin Film Structures of Regioregular Poly (3-hexyl thiophene) Using Volatile Solvents. *Appl. Phys. Lett.* **2007**, *90*, 172116.
- (57) Kawano, K.; Sakai, J.; Yahiro, M.; Adachi, C. Effect of Solvent on Fabrication of Active Layers in Organic Solar Cells Based on Poly (3-hexylthiophene) and Fullerene Derivatives. *Sol. Energy Mater. Sol. Cells* **2009**, 93, 514–518.
- (58) Keum, J. K.; Xiao, K.; Ivanov, I. N.; Hong, K.; Browning, J. F.; Smith, G. S.; Shao, M.; Littrell, K. C.; Rondinone, A. J.; Payzant, E. A.; et al. Solvent Quality-Induced Nucleation and Growth of Parallelepiped Nanorods in Dilute Poly (3-hexylthiophene)(P3HT) Solution and The Impact on The Crystalline Morphology of Solution-Cast Thin Film. *CrystEngComm* **2013**, *15*, 1114–1124.
- (59) Scharber, M. C.; Mühlbacher, D.; Koppe, M.; Denk, P.; Waldauf, C.; Heeger, A. J.; Brabec, C. J. Design rules for donors in bulk-heterojunction solar cells—Towards 10% energy-conversion efficiency. *Adv. Mater.* **2006**, *18*, 789–794.
- (60) Kirchartz, T.; Taretto, K.; Rau, U. Efficiency Limits of Organic Bulk Heterojunction Solar Cells. *J. Phys. Chem. C* **2009**, *113*, 17958–17966.
- (61) Voroshazi, E.; Verreet, B.; Aernouts, T.; Heremans, P. Longterm operational lifetime and degradation analysis of P3HT:PCBM photovoltaic cells. *Sol. Energy Mater. Sol. Cells* **2011**, 95, 1303–1307.
- (62) Cao, H.; He, W.; Mao, Y.; Lin, X.; Ishikawa, K.; Dickerson, J. H.; Hess, W. P. Recent progress in degradation and stabilization of organic solar cells. *J. Power Sources* **2014**, 264, 168–183.
- (63) Hoppe, H.; Niggemann, M.; Winder, C.; Kraut, J.; Hiesgen, R.; Hinsch, A.; Meissner, D.; Sariciftci, N. S. Nanoscale Morphology of Conjugated Polymer/Fullerene-Based Bulk-Heterojunction Solar Cells. *Adv. Funct. Mater.* **2004**, *14*, 1005–1011.
- (64) Chen, D.; Nakahara, A.; Wei, D.; Nordlund, D.; Russell, T. P. P3HT/PCBM Bulk Heterojunction Organic Photovoltaics: Correlating Efficiency and Morphology. *Nano Lett.* **2011**, *11*, 561–567.
- (65) Wang, H.; Wang, H.-Y.; Gao, B.-R.; Wang, L.; Yang, Z.-Y.; Du, X.-B.; Chen, Q.-D.; Song, J.-F.; Sun, H.-B. Exciton Diffusion and Charge Transfer Dynamics in Nano Phase-Separated P3HT/PCBM Blend Films. *Nanoscale* **2011**, *3*, 2280–2285.